






Electro-optic properties of ZrO_2 , HfO_2 , and LiNbO_3 ferroelectric phases: A comparative density functional study

Ali El Boutaybi ^{1,*}, Panagiotis Karamanis,² Thomas Maroutian ¹, Sylvia Matzen ¹, Laurent Vivien ¹, Philippe Lecoer,¹ and Michel R  rat ²

¹Centre de Nanosciences et de Nanotechnologies (C2N), Universit   Paris-Saclay, CNRS, 91120 Palaiseau, France

²Universit   de Pau et des Pays de l'Adour, CNRS, IPREM, E2S UPPA, Pau, France



(Received 27 September 2022; revised 7 December 2022; accepted 3 January 2023; published 27 January 2023)

We report the Pockels electro-optic properties of ZrO_2 and HfO_2 orthorhombic $Pbc2_1$ and rhombohedral $R3m$ ferroelectric phases, and we compare them to the well-known rhombohedral $R3c$ LiNbO_3 Pockels material from density functional theory calculations using the CRYSTAL suite of programs. Specifically, three essential processes are explicitly investigated: The electronic, the ionic (or vibrational), and the piezoelectric contributions. Our calculations reveal that the ionic part coming from the low-frequency phonon modes contributes the most to the electro-optic coefficients of rhombohedral LiNbO_3 and of orthorhombic ZrO_2 and HfO_2 . Additionally, the low-frequency phonon modes exhibit zero contribution to the Pockels coefficients of ZrO_2 and HfO_2 rhombohedral $R3m$ phase.

DOI: [10.1103/PhysRevB.107.045140](https://doi.org/10.1103/PhysRevB.107.045140)

I. INTRODUCTION

Silicon photonics platforms are becoming indispensable for developing low-cost integrated photonic circuits. The electro-optic (EO) effect is one of the main properties required in a plethora of applications, including optical communications [1–4], quantum computing [5,6], and neuromorphic applications [7–9]. The principal physical process behind these applications is the so-called Pockels or linear EO effect, which is related to the modulation of the refractive index of a material under an applied external electric field [10]. Nevertheless, due to its centrosymmetric atomistic crystalline structure, pristine silicon features vanishing second-order optical nonlinearities; thus, it is unsuitable for EO applications. Bearing in mind that second-order nonlinear optical (NLO) responses strictly manifest in noncentrosymmetric materials, ferroelectric (FE) crystalline solids have emerged as the main materials of choice in EO applications. Such materials exhibit an intrinsic electric polarization that, in addition, can be controlled and tuned in a reversible manner by the application of an external electric field.

In the realm of EO applications, the most studied FE materials are currently ABO_3 perovskite-type crystalline solids. A representative member of this family is tetragonal ferroelectric barium titanate (BaTiO_3 , BTO), featuring one of the highest Pockels bulk coefficients ($r_{42} \approx 1300$ pm/V) [11]. The growth of high-quality BTO thin films on silicon without affecting its strong Pockels coefficient is still challenging and of high cost. However, high-quality BTO films can be fabricated via molecular beam epitaxy (MBE) [4,12,13]. In addition to tetragonal BTO, its rhombohedral $R3m$ phase also gained attention for cryogenic technologies such as, for instance,

quantum computing [14,15]. Another well-studied material is lithium niobate [LiNbO_3 (LNO)], a ferroelectric material featuring a strong Pockels crystalline bulk coefficient (r_{33}) of about 30 pm/V [16]. LNO is widely applied in the telecommunications industry [17] and specifically in the fabrication of optical modulators. Despite LNO's complexity of integration on silicon substrates, several studies showed its compatibility with silicon photonics [18,19].

Recently, it has been demonstrated that among HfO_2 - ZrO_2 -based thin films, orthorhombic $Pbc2_1$ [20] and rhombohedral $R3m$ [21] phases exhibit ferroelectric behavior. This is a significant finding in terms of practical applications because both HfO_2 and ZrO_2 have excellent silicon compatibility [22–25]. Combined with their ferroelectric nature, this might lead to significant breakthroughs in the realm of integrated photonic circuits that could significantly reduce the fabrication cost. Nevertheless, there is still much work to be done since the film quality and the ferroelectricity of ZrO_2 and HfO_2 are not well optimized at high film thicknesses. This is critical for their optimal application due to the inverse proportionality between the optical losses and the film thickness [26,27]. In the case of the orthorhombic $Pbc2_1$ (o -phase), which is usually reported in polycrystalline thin films, ferroelectricity has been demonstrated in a large range of thickness from 1 nm to 1 μm [28–31]. This o -phase has also been reported in epitaxial thin films with a thickness less than 20 nm [32–34]. Regarding the rhombohedral $R3m$ (r -phase), the reported thicknesses ranged from 5 to 40 nm [21,35,36]. Indeed, for applications, ultrathin films are often advantageous, e.g., in the case of nonvolatile memories and ferroelectric field-effect transistors [22,23], energy storage [24,25], negative capacitance [37,38], and tunnel junctions [39,40].

In terms of NLO properties, the studies on ZrO_2 - HfO_2 materials are scarce, leaving open the question of the potential of these compounds for optical applications. Indeed,

*ali.el-boutaybi@c2n.upsaclay.fr

to our knowledge, only two experimental studies can be found in the literature [41,42]. They investigate the EO effect in Y_2O_3 -doped HfO_2 , reporting an EO coefficient of about 0.67 pm/V for (111)-oriented thin films, a modest value compared to the ones in trigonal LNO and perovskite BTO materials. However, the exact EO coefficients of the two experimentally reported ferroelectric phases in HfO_2 and ZrO_2 are not known yet. Therefore, the primary objective here is to report and investigate the EO coefficients of HfO_2 and ZrO_2 materials.

In this work, we study the second-order nonlinear optical (NLO) properties of the orthorhombic $Pbc2_1$ and rhombohedral $R3m$ phases of ZrO_2 and HfO_2 , relying on all-electron density functional theory (DFT) computations to report reliable EO coefficients. The obtained results are compared to the ones computed for the rhombohedral $R3c$ LNO phase, for which experimental data are available, allowing us to use LNO as a reference material. All reported EO coefficients have been determined from the microscopic second-order NLO responses of these systems, which, in turn, have been obtained via a coupled perturbed Kohn-Sham (CPKS) and Hartree-Fock (CPHF) analytical approach developed and implemented in the CRYSTAL17 suite of quantum chemical programs by one of the authors of this study [43]. It has already been established that this perturbative approach delivers high-accuracy molecular and bulk electric properties, free from numerical errors [44,45]. To achieve the maximum possible relevance with the available or future experimental data, the reported coefficients comprise electronic, vibrational, and piezoelectric contributions, which have also been obtained analytically. Especially for comparison between theory and experiment, such contributions are of essential importance for a reliable prediction of the overall NLO response of a given crystalline or molecular material and the complete understanding of its origin.

Our article is organized as follows: First, we give the theoretical background of our study, insisting on the close relationship between the macroscopic NLO susceptibilities and the microscopic hyperpolarizabilities of the unit shells. Then, we study the EO properties of LNO using CRYSTAL code, which will serve as the material of reference. Specifically, we report reliable values of its microscopic second-order responses, and we analyze the electronic, vibrational, and piezoelectric contributions. Finally, we report and discuss the Pockels EO coefficients of the o - and r -phase of ZrO_2 and HfO_2 , comparing them to those calculated for the $R3c$ rhombohedral phase of LNO.

II. THEORETICAL FRAMEWORK AND COMPUTATIONAL DETAILS

The microscopic linear and nonlinear optical properties of a finite zero-dimensional system are defined in terms of a Taylor power series expansion with respect to an external applied electric field E_{jkl} as

$$\mu_i = \mu_0 + \alpha_{ij}^{\text{tot}} E_j + \frac{1}{2} \beta_{ijk}^{\text{tot}} E_j E_k + \frac{1}{6} \gamma_{ijkl}^{\text{tot}} E_j E_k E_l + \dots, \quad (1)$$

where i, j, k , and l stand for Cartesian coordinates (x, y, z) , μ_i and μ_0 are the induced and the permanent dipole moment, α_{ij}^{tot} is the total dipole electric polarizability, while β_{ijk}^{tot} and

$\gamma_{ijkl}^{\text{tot}}$ are the total first and second dipole hyperpolarizabilities, respectively. By the term total (tot) it is implied that both electronic (ele) and vibrational (vib) contributions [44–46] are taken into account, hence

$$\alpha_{ij}^{\text{tot}} = \alpha_{ij}^{\text{ele}} + \alpha_{ij}^{\text{vib}}, \quad (2)$$

$$\beta_{ijk}^{\text{tot}} = \beta_{ijk}^{\text{ele}} + \beta_{ijk}^{\text{vib}}. \quad (3)$$

For three-dimensional periodic crystalline lattices, Eq. (1) can be written as

$$P_i = P_0 + \chi_{ij}^{(1)} E_j + \chi_{ijk}^{(2)} E_j E_k + \chi_{ijkl}^{(3)} E_j E_k E_l + \dots, \quad (4)$$

where P_i is the unit-cell induced polarization, while $\chi_{ij}^{(1)}$, $\chi_{ijk}^{(2)}$, and $\chi_{ijkl}^{(3)}$ stand for the total first-order (linear), and the second- and third-order (nonlinear) optical macroscopic bulk susceptibilities, respectively. The first and second coefficients of Eq. (4) are deduced from the total microscopic (hyper)polarizabilities per unit cell in atomic units as follows:

$$\chi_{ij}^{(1)} = \frac{4\pi}{V} \alpha_{ij}^{\text{tot}}, \quad (5)$$

$$\chi_{ijk}^{(2)} = \frac{2\pi}{V} \beta_{ijk}^{\text{tot}}, \quad (6)$$

where V is the unit-cell volume.

The theoretical background of the above relations can be found in [45,47–50]. The total first-order susceptibility $\chi_{ij}^{(1)}$ can be used to deduce the relative dielectric tensor ϵ_{ij} , which in turn gives access to bulk refractive indices n_{ii} via the following expressions:

$$\epsilon_{ij} = \delta_{ij} + \chi_{ij}^{(1)}, \quad (7)$$

$$n_{ii} = \epsilon_{ii}^{1/2}. \quad (8)$$

In the above equations, δ_{ij} represents the elements of the identity matrix ($\delta_{ij} = 1$ for $i = j$, and 0 for $i \neq j$). Note that we consider in this work a diagonal ϵ_{ij} tensor so that the subscript i of ϵ_{ii} corresponds to one of the three principal axes n_{ii} of the ellipsoidal indicatrix.

Now, to obtain the EO Pockels coefficients (r_{ijk}), as a first step we consider the constant stress (or “clamped”) conditions, wherein $\chi_{ijk}^{(2)}$ and the bulk refractive indices n_{ii} given in Eq. (8) can be used to determine one out of the two terms contributing to the total r_{ijk} coefficients. The clamped EO coefficient is denoted here as r_{ijk}^S , comprising both vibrational and electronic contributions, and it is defined as

$$r_{ijk}^S = -2 \frac{\chi_{ijk}^{(2)}}{n_{ii}^2 n_{jj}^2}. \quad (9)$$

In the second step, we should model and consider the relevant acoustic contribution stemming from the piezoelectric effect. This effect depends on the frequency of the applied ac electric field as it originates from the inverse piezoelectric effect, according to which the application of an ac oscillating field induces mechanical deformations on the crystalline lattice. The resulting contribution to the r_{ijk} coefficients, denoted here as r_{ijk}^P , is defined from the photoelastic tensor $\mathbb{P}_{ij\mu\nu}$ and

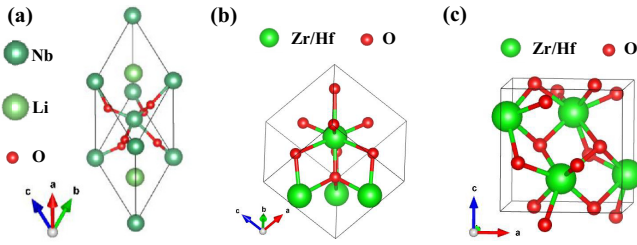


FIG. 1. The crystallographic structures of (a) LiNbO₃ (space group *R3c*), (b) rhombohedral ZrO₂-HfO₂ (space group *R3m*), and (c) orthorhombic ZrO₂-HfO₂ (space group *Pbc2*₁).

the piezoelectric strain coefficients $d_{k\mu\nu}$ [51,52] as

$$r_{ijk}^p = \sum_{\mu, \nu=1}^3 \mathbb{P}_{ij\mu\nu} d_{k\mu\nu}. \quad (10)$$

The calculation of the tensorial components of r_{ijk}^p is achieved via the computation of the photoelastic constants $\frac{\partial \eta_{ij}}{\partial S_{\mu\nu}}$ ($\mathbb{P}_{ij\mu\nu}$) defined as the derivative of the impermeability tensor η_{ij} (given by the inverse dielectric tensor ϵ_{ij}^{-1}) with respect to strain $S_{\mu\nu}$, which are the elements of the fourth rank photoelastic tensor and of the piezoelectric strain coefficients $\frac{\partial S_{\mu\nu}}{\partial E_k}$ ($d_{k\mu\nu}$) [53]. Finally, the total EO coefficients that we report in this work are calculated as $r_{ijk} = r_{ijk}^S + r_{ijk}^p$. More detailed information about photoelastic calculations can be found elsewhere [51–53].

All computations of frequency-dependent properties have been performed with the CRYSTAL suite of programs [43]. To determine the dynamic vibrational and electronic (clamped nuclei) hyperpolarizabilities, a fully analytical approach relying on the coupled perturbed Hartree-Fock and Kohn-Sham method (CPHF/CPKS) has been applied [44,45,54–56]. In the case of LNO, we considered three different DFT functionals to investigate the dependence on the DFT method of the properties of interest and to compare the results with available experimental data. That includes the Becke, three-parameter, Lee-Yang-Parr exchange-correlation functional (B3LYP) [57,58], the pure Perdew-Burke-Ernzerhof one (PBE) [59], and with 25% Hartree-Fock (HF) exchange (PBE0) [60]. In the case of ZrO₂ and HfO₂ (orthorhombic *Pbc2*₁ and rhombohedral *R3m* phases), only the B3LYP functional has been applied as it gives good results for LNO. The basis sets of LNO are taken from Refs. [61–63] for Nb, Li, and O, respectively. The basis sets for ZrO₂ are from Refs. [62,64] for O and Zr, respectively, while those for HfO₂ are taken from Refs. [65,66] for O and Hf, respectively.

III. RESULTS AND DISCUSSION

A. LNO rhombohedral *R3c*

We chose to start our investigation with LNO, which features a ferroelectric *R3c* ground state at low temperatures. The crystal structure of the bulk system, built from 10 atoms per unit cell, is shown in Fig. 1(a) [lattice constants and atomic coordinates are given in Table S.1 in the Supplemental Material (SM) [67]]. Computed band gaps, dynamic refractive indices n_{ii} , and ϵ_{ii} values of LNO determined with three functionals

TABLE I. Band gap, refractive indices n_{ii} , birefringence δn , and dielectric constants ϵ_{ii} of LNO calculated at a 633 nm wavelength using different functionals and compared to experimental results. Values in parentheses correspond to the static values (at “infinite” wavelength).

	B3LYP	PBE0	PBE	LDA [73]	Expt. [71]	Expt. [74]
Gap (eV)	4.75	5.29	3.15		3.78	
n_{xx} (n_o)	2.257	2.227	2.497	2.37	2.28	2.286
n_{zz} (n_e)	2.149	2.120	2.402	2.35	2.18	2.202
δn	0.107	0.107	0.095	/	0.098	0.09
ϵ_{xx}	5.10 (4.71)	4.96	6.23	/	/	/
ϵ_{zz}	4.63 (4.31)	4.50	5.77	/	/	/

of different types at an optical frequency corresponding to 633 nm wavelength are listed in Table I. Apart from electronic contributions, which can be trivially computed with the CPKS approach, the reported values comprise as well the respective vibrational contributions computed at the same level of theory. The wavelength of 633 nm was chosen in order to directly compare our results to available data reported in the literature. Note that the EO properties are also investigated up to the near-infrared wavelength range in Sec. III B.

Starting from the computed band gap of LNO, it is seen that out of the three methods used, B3LYP and PBE0 yield notably larger values as compared to the reported experimental values. On the other hand, the pure PBE functional follows the opposite trend. The frequently cited direct band-gap value of LNO, mostly concluded from optical experiments [68], is about 3.78 eV. However, this value should be considered with care due to electron-hole attraction effects, which might induce important underestimations in the final outcome of optical measurements, as already discussed in Refs. [69,70]. Therefore, for LNO crystal, a band gap of 4.7 eV [69] should be considered more suitable for comparison between theory and experiment, close to the value calculated with the B3LYP functional and the associated basis set.

Turning our attention to the refractive indices computed in this study, we also notice that both B3LYP and PBE0 functionals yield values that fall very close to the available experimental measurements. On the other hand, pure PBE overshoots the experimental reference values, yielding values close to the earlier local-density approximation (LDA) reported results. This behavior is not surprising since pure DFT functionals generally underestimate the gap, returning overestimated cell polarizabilities α_{ij} [46] and dielectric constants. Hence, it is expected to affect the refractive indices [Eq. (8)]. Nonetheless, despite the apparent deviations in functional performance, all methods considered predict relatively stable birefringence values (denoted δn in Table I), in good agreement with the available experimental measurements conducted on stoichiometric LNO crystals (cationic ratio Li/Nb ~ 1) [71,72].

The clamped EO coefficients r_{ijk}^S of LNO, together with the corresponding electronic and vibrational contributions computed with the B3LYP functional, are listed in Table II. We also list previously published experimental measurements and theoretical data in the same table. All properties have been

TABLE II. $r_{ijk}(-\omega_\sigma; \omega, 0)$ EO tensor (pm/V) of LNO at 633 nm wavelength: electronic and ionic (clamped) and piezoelectric (unclamped) contributions, together with results from previous calculations and experiments.

	B3LYP		LDA [73]		Expt. [16]	Expt. [77]	
Clamped	r_{33}^{ele}	r_{33}^{vib}	r_{33}^S				
	r_{33}	7.19	23.45	30.64	26.9	30.8	34
	r_{13}	2.74	7.94	10.68	9.7	8.6	10.9
	r_{11}	-1.02	-6.84	-7.86	4.6	3.4	/
	r_{51}	3.08	19.43	22.51	14.9	28	/
Unclamped	r_{ijk}^p		r_{ijk}		[78]	Expt. [79]	
	r_{33}	1.50	32.14	27	32.2	/	
	r_{13}	1.42	12.10	10.5	10	/	
	r_{11}	0.86	-7.00	7.5	6.8	9.9	
	r_{51}	10.77	33.28	28.6	32.6	/	

deduced from computed $\chi_{ijk}^{(2)}(-\omega_\sigma; \omega, 0)$ (for the Pockels coefficient calculation, ω stands for a laser wavelength, $\omega = 0$ for a static electric field, and ω_σ is the sum of two wavelengths; see the SM for more details [67]) obtained at the same level of theory, considering only the four EO independent tensorial components of LNO r_{33} , r_{13} , r_{11} , and r_{51} [73,75]. In brief, the so-called vibrational (or ionic) contribution comes from transverse optical (TO) phonon modes; they can be represented as $4A_1 + 5A_2 + 9E$, where the A_1 and E modes are Raman- and infrared- (IR) active; in contrast, A_2 modes are silent. The A_1 modes are expected to contribute to r_{33} and r_{13} , while the E modes are linked to r_{11} and r_{51} . The corresponding computed phonon frequencies, showing a good agreement with available experimental data, together with the second-order nonlinear susceptibilities $\chi_{ijk}^{(2)}(-\omega_\sigma; \omega, 0)$ at a wavelength of 633 nm, are given in the SM [67]. Looking at the computed clamped EO coefficients presented in Table II, the results obtained with the B3LYP functional are in very good agreement with experimental results, notably for r_{33} and r_{13} coefficients. On the other hand, an overestimation of r_{11} and an underestimation of r_{51} , respectively, are revealed. Moreover, we evidenced that the values obtained for these two particular coefficients strongly depend on the choice of the functional (Table S5 [67]). With the LDA framework, as implemented in the CRYSTAL suite of programs, we found results close to the previous LDA calculations done with the linear response theory using atomic potentials [73,75]. We note that the latter approach led to systematically lower absolute values of coefficients with respect to CPHF computations conducted with hybrid density functionals (Table S5 [67]).

Our calculations expose that the most dominant contribution out of the two considered for r_{ijk}^S is the vibrational contribution to the microscopic second hyperpolarizability of the unit cell. The approach used here for EO calculations also provides further insights into this ionic contribution computed by evaluating the Raman and IR intensities [45], as described in Refs. [56,76]. The lowest frequency A_1 and E polar phonon modes (graphic representations of these phonons are given in Fig. S2 [67]) are found to contribute the most to r_{33}^S and r_{51}^S , respectively, amounting to 33% and 32% of these EO coefficients. These results, relying on a hybrid DFT treatment

of the wave function, confirm previous computations within the LDA approximation [73].

We now consider the total unclamped EO coefficients r_{ijk} of LNO, including the piezoelectric contribution, which is computed at the same level of theory as discussed above. We note that the photoelastic constants $\mathbb{P}_{ij\mu\nu}$, here computed at 633 nm, are found to be relatively independent of the wavelength above 633 nm (see Fig. S.2 [67]). The same trend has been observed for MgO and CaWO₄ crystals from calculations at the PBE level [51,53]. The piezoelectric contribution to the EO coefficients is listed in Table II as r_{ijk}^p . Looking at the total $r_{ijk} = r_{ijk}^S + r_{ijk}^p$, an excellent agreement with experimental results is obtained. For the three coefficients r_{33} , r_{13} , and r_{11} , the vibrational contribution is still by far the dominant one, while the r_{51} coefficient has the highest piezoelectric contribution (Table II). Three functionals, B3LYP (Table II), PBE0, and PBE (Table S5 [67]), give a piezoelectric contribution to r_{51} of around 11 pm/V, which represents around 33% of the r_{51} unclamped value, lower than the 48% found in Ref. [73]. Nevertheless, the r_{51} EO coefficient is found with the highest piezoelectric contribution from the four independent EO coefficients of LNO material, in line with the previous theoretical results [73]. Experimentally, a piezoelectric contribution to r_{51} of only 4.6 pm/V has been reported [16]. This disagreement might be due to the experimental method, which cannot suppress the total piezoelectric contribution during the measurement of the clamped coefficient, as previously suggested in Ref. [73]. Again, we found that the choice of the functional strongly affects both the magnitude and sign of the piezoelectric contribution to r_{11} (Table S5 [67]). In particular, the B3LYP functional gives an opposite piezoelectric contribution to the total r_{11} coefficient, reducing its absolute value but keeping it close to the reported experimental one (Table II). Finally, our B3LYP calculations produced a very good estimation of the EO tensorial components of LNO with respect to the experimental data.

B. ZrO₂-HfO₂ orthorhombic *Pbc2₁*

In this section, we present electro-optic properties of the *o*-phase of ZrO₂ and HfO₂ compounds, with space group *Pbc2₁* (no. 29). The lattice optimization of *Pbc2₁* ZrO₂ and HfO₂ has been performed using a 12-atom unit cell. The optimized crystalline structure and atomic positions are given in the SM [67]. The polarization, defined as the electric dipole moment per unit volume, was also computed for *o*-phase ZrO₂ and HfO₂ via Berry phase calculation using QUANTUM ESPRESSO (QE) [80] in order to verify that the optimized polar phases are consistent with the ones reported in the literature [20,81]. Table III displays the band gap, refractive indices, and polarization of *o*-phase ZrO₂ and HfO₂. Although no experimental data are available for comparison with respect to the optical properties of these systems, the polarizations obtained here are very close to the ones reported in previous studies [81].

It is well known that ZrO₂ and HfO₂ compounds have a wide band gap, as they are used for high-*k* applications. From Table III, it can be seen that the band gap of *o*-HfO₂ is larger by about 1 eV than in *o*-ZrO₂. Another feature is that the refractive indices at 633 nm of *o*-ZrO₂ are found to be higher than the ones of *o*-HfO₂. This is interesting since

TABLE III. Band gap and refractive indices of orthorhombic $Pbc2_1$ ZrO₂ and HfO₂ at 633 nm computed at B3LYP level of theory. The polarization P_b (along the b axis) from Berry phase calculation with the PBE functional is also shown. All computations have been carried out on B3LYP optimized unit cells.

	o -ZrO ₂	o -HfO ₂
Gap (eV)	5.40	6.45
n_{xx}	2.204	2.059
n_{yy}	2.301	2.122
n_{zz}	2.236	2.081
P_b ($\mu\text{C}/\text{cm}^2$)	54 (58 [81])	49.5 (50 [81])

a high refractive index is an essential element for silicon photonic applications in order to ensure a sufficient contrast with the refractive index of SiO₂ [12]. We also have to consider the vibrational modes of the $Pbc2_1$ phase, as these modes are directly linked and contribute to the EO coefficients. The primitive unit cell of $Pbc2_1$ phase with 12 atoms (four formula units) results in 36 vibrational modes, 3 for translation modes and 33 for optical modes, having the following irreducible representation at the Γ point:

$$\Gamma = 8A_1 + 9A_2 + 8B_1 + 8B_2. \quad (11)$$

The A_1 , B_1 , and B_2 modes are Raman- and IR-active. Hence, they are expected to contribute to the electro-optic coefficients, while A_2 modes are only Raman-active. For the sake of clarity, Table IV lists only the calculated A_1 phonon frequencies, while the remaining phonon frequencies (A_2 , B_1 , B_2) are given in the SM [67]. Unfortunately, only a few experimental phonon frequencies of $Pbc2_1$ o -phase are available for pure ZrO₂ and HfO₂. They are all displayed for o -ZrO₂ in Table IV, showing a good agreement with our calculated phonon modes. Orthorhombic $Pbc2_1$ belonging to a 2 mm point group of symmetry features five independent EO coefficients [83]: r_{13} , r_{23} , r_{33} , r_{42} , and r_{51} . The relevant vibrational contributions should come from modes A_1 , B_1 , and B_2 . Specifically, A_1 modes should contribute to r_{13} , r_{23} , and r_{33} components, while B_1 and B_2 modes are expected to affect r_{42} and r_{51} , respectively. These five EO coefficients are computed at the same level of theory as discussed for LNO, and they are listed in Table V showing the three different contributions, electronic r_{ijk}^{ele} , vi-

TABLE IV. Calculated frequencies (cm^{-1}) of Raman- and IR-active A_1 phonon modes of ferroelectric ZrO₂ and HfO₂ using B3LYP functional.

	o -ZrO ₂	o -HfO ₂	r -ZrO ₂	r -HfO ₂
	expt. [82]			
A_1	102	/	113	171
	186	200	153	220
	291	/	253	267
	315	320	295	352
	351	340	329	449
	387	/	369	534
	445	/	451	674
	566	580	589	775
			755	770

TABLE V. The five independent elements of $r_{ijk}(-\omega_\sigma; \omega, 0)$ tensor for $Pbc2_1$ space group, together with their respective electronic, vibrational, and piezoelectric contributions, computed at a wavelength of 633 nm. All values are given in pm/V.

	o -ZrO ₂				o -HfO ₂			
	r_{ijk}^{ele}	r_{ijk}^{vib}	r_{ijk}^{p}	r_{ijk}	r_{ijk}^{ele}	r_{ijk}^{vib}	r_{ijk}^{p}	r_{ijk}
r_{33}	2.10	8.75	0.5	11.35	1.52	5.56	0.14	7.22
r_{13}	-1.49	-9.29	-1.38	-12.17	-0.81	-6.32	-0.83	-7.96
r_{23}	-0.51	-2.19	0	-2.70	-0.51	-1.94	0	-2.58
r_{42}	-0.53	-0.95	0	-1.48	-0.54	-0.83	0	-1.37
r_{51}	-1.00	-1.16	0	-2.16	-0.83	-0.94	0	-1.77

brational r_{ijk}^{vib} , and piezoelectric r_{ijk}^{p} . The first significant result is that the EO coefficients in o -ZrO₂ are almost two times larger than the ones obtained for o -HfO₂. Coefficients r_{13} and r_{33} exhibit the highest values out of the five independent EO tensorial elements. Either for ZrO₂ or HfO₂, these two coefficients have opposite signs and are quite close in absolute value. Comparing the calculated EO results of o -ZrO₂ to those of the reference LNO material (Table II), r_{13} of o -ZrO₂ is close to r_{13} of LNO, while r_{33} of o -ZrO₂ is about one-third the coefficient of LNO. Unfortunately, no experimental results are available for pure o -ZrO₂ and o -HfO₂. The only EO experimental data, to the best of our knowledge, are the effective coefficients reported by Kindo *et al.* [41,42] for Y₂O₃-doped HfO₂ o -phase measured in (100) (0.46 pm/V) and (111) (0.67 pm/V) oriented thin films.

From the values listed in Table V, we also deduce that, as in LNO, the vibrational contribution dominates the values of the EO coefficients in o -phase ZrO₂ and HfO₂. For example, the lowest frequency A_1 TO mode at 102 cm^{-1} (Table IV) is responsible for about 40% and more than 60% of the total values of r_{33} and r_{13} in o -ZrO₂, respectively (the displacement patterns of these phonon modes are shown in Fig. S2 [67]). This is similar to what we observed in the case of LNO, with low phonon modes highly contributing to the EO coefficients. Note that, in LNO, unstable phonon modes in the paraelectric phase transform into lower frequency and highly polar modes in the low-temperature ferroelectric phase. Thus, these low phonon modes significantly contribute to the EO coefficients of LNO [73], but a similar explanation has not been evidenced for ZrO₂ and HfO₂. Indeed, these materials have numerous polymorphs [84], and other mechanisms are responsible for ferroelectric phase formation [81,85], away from the classical paraelectric-ferroelectric phase transition picture.

Wavelength dependence of EO coefficients

The EO values reported above are computed at 633 nm in order to compare our results to the available experimental data. However, wavelengths for telecom applications are in the near-infrared region, typically around 1500 nm. Therefore, focusing on the influence of laser wavelength on Pockels coefficients, the same calculations as performed at 633 nm were repeated at different wavelengths up to near-infrared. The results are displayed in Fig. 2 for the unclamped r_{33}

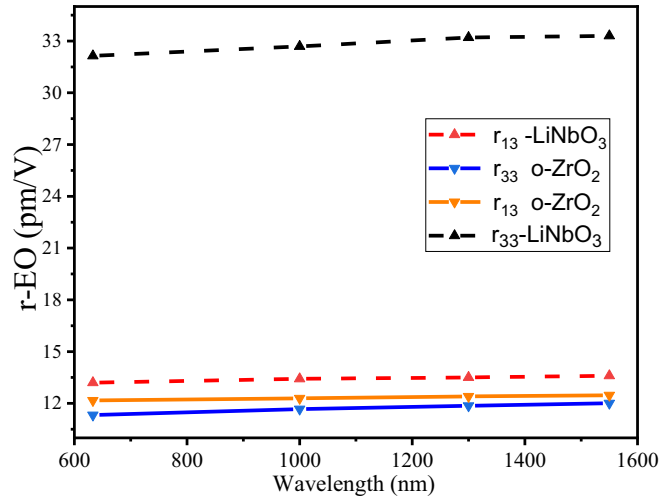


FIG. 2. EO coefficients (unclamped) r_{33} and r_{13} of LNO and o -ZrO₂ at different wavelengths using B3LYP functional.

and r_{13} coefficients of LNO and o -ZrO₂. ZrO₂ is chosen here instead of HfO₂ because of its higher EO coefficients compared to HfO₂ (Table V). As seen on the graph, the wavelength of the incident light marginally affects the total values of the studied EO coefficients. Among the three wavelength-dependent contributions to the EO coefficients, the electronic part is expected to be more sensitive to the electric field than the vibrational and piezoelectric contributions. Specifically, approaching the IR wavelengths, the electronic contribution decreases and converges to a static value [44,45]. This decrease is associated with a decrease of the refractive indices: At a wavelength of 1550 nm, the refractive index n_{zz} is found to be 2.08 (2.19) for LNO (for ZrO₂), which is lower than the value obtained at 633 nm (Tables I and III). On the other hand, vibrational contributions remain almost constant from 633 to 1550 nm. A similar trend is obtained for the piezoelectric contribution, which depends on the wavelength via the photoelastic coefficients. As shown in Fig. S1 [67], the latter coefficients remain relatively constant at high wavelengths. Hence, the overall weak increase of the total EO coefficients observed in Fig. 2 when increasing the wavelength should be mostly attributed to the decrease of the refractive indices [see Eq. (9)].

By comparing the EO coefficients of o -ZrO₂ with those of LNO, it becomes evident that the former features weaker responses at all investigated wavelengths. Nevertheless, in terms of applications, other parameters should be taken into consideration, such as the refractive index and the total dielectric constant, to define a figure of merit ($n^3 r_{ijk}/\epsilon$ [27], with ϵ the dielectric constant comprising both the electronic and the ionic contributions) that could bring o -phase ZrO₂/HfO₂ as a competitive material for EO applications. Figure 3 displays a visual comparison of this figure of merit between LNO, HfO₂, and ZrO₂ materials. For r_{33} coefficient, LNO has the highest figure of merit; however, the ones for ZrO₂ and HfO₂ are not negligible. Considering the compatibility of ZrO₂ and HfO₂ with silicon, these results are significant enough to stimulate further investigation on the different paths to increase the EO coefficients in these materials.

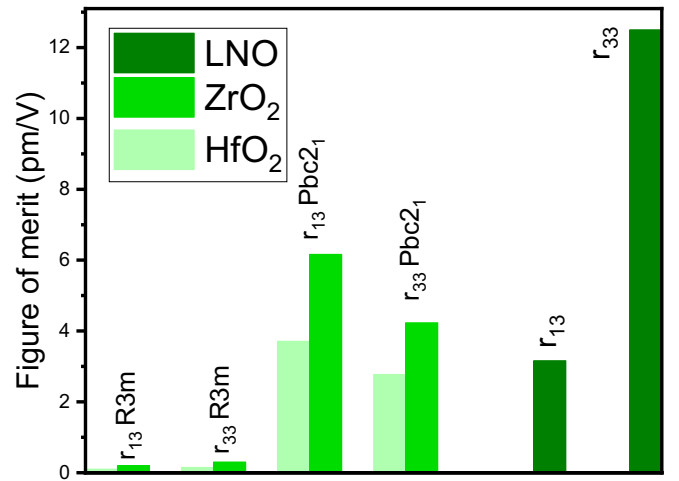


FIG. 3. Figure of merit ($n^3 r_{ijk}/\epsilon$) of HfO₂ and ZrO₂ compared to LNO using r_{33} and r_{13} coefficients.

C. ZrO₂-HfO₂ rhombohedral $R3m$

Here, we focus on the EO properties of the rhombohedral $R3m$ (space group no. 160) phase of ZrO₂-HfO₂. This phase is less studied than the orthorhombic phase and has only been reported in compressively strained epitaxial thin films [21,36]. For the EO calculations, we also used a unit cell of 12 atoms (4 formula units). One should note that in the case of the r -phase, an instability (expressed by negative/imaginary frequency) of A_1 -TO₁ phonon mode was observed at the equilibrium geometry of the optimized unit-cell volume for r -ZrO₂ (141 Å³) and r -HfO₂ (136 Å³), the optimized unit cells being given in the SM [67]. For the calculation of EO coefficients and other properties to be reliable, one should have only real frequencies. To achieve such a condition for ZrO₂, an experimental volume (~ 132 Å³) was imposed together with a rhombohedral angle equal to 89.56° [36]. Under such geometry constraints, the imaginary phonon mode calculated at 82i cm⁻¹ becomes real at 76 cm⁻¹. For HfO₂, no r -phase unit-cell volume has been experimentally reported yet; thus, we manually reduced its volume until we reached a unit cell characterized by real phonon frequencies. At the respective level of theory, the corresponding volume amounts to 128 Å³.

The computed band gap, refractive indices, and polarization are displayed in Table VI. The band gaps obtained for ZrO₂ and HfO₂ in the r -phase are significantly higher than in

TABLE VI. Band gap and refractive indices of rhombohedral $R3m$ ZrO₂ and HfO₂ at 633 nm computed with the B3LYP functional. The polarization P_r from Berry phase calculation with the PBE functional is also shown. All computations have been carried out on B3LYP-optimized unit cells.

	r -ZrO ₂	r -HfO ₂
Gap (eV)	5.79	6.77
n_{xx}	2.282	2.114
n_{zz}	2.271	2.107
δn	0.011	0.007
P_r ($\mu\text{C}/\text{cm}^2$)	6.8	5.1

TABLE VII. The four independent elements of $r_{ijk}(-\omega_\sigma; \omega, 0)$ tensor for $R3m$ space group, together with their respective electronic, vibrational, and piezoelectric contributions, computed at a wavelength of 633 nm. All values are given in pm/V.

	$r\text{-ZrO}_2$				$r\text{-HfO}_2$			
	r_{ijk}^{ele}	r_{ijk}^{vib}	r_{ijk}^p	r_{ijk}	r_{ijk}^{ele}	r_{ijk}^{vib}	r_{ijk}^p	r_{ijk}
r_{33}	-0.11	-0.30	-0.01	-0.42	-0.07	-0.21	-0.02	-0.30
r_{13}	0.05	0.14	0.05	0.24	0.03	0.13	0.11	0.27
r_{11}	-0.06	-0.21	-0.20	-0.28	-0.05	-0.08	-0.16	0.29
r_{51}	0.05	0.08	-0.25	-0.12	0.03	0.21	-0.19	0.05

the o -phase. The polarization of either ZrO₂ or HfO₂ is found to be lower than the one obtained in the o -phase, as expected from previous calculations [21,35]. Note that this polarization depends strongly on the compressive strain, which is directly related to the rhombohedral angle [21,36]. Here, the polarization is computed at a fixed angle using the rhombohedral primitive unit cell. In contrast, in Refs. [21,35] the polarization is computed with hexagonal unit cells and at different compressive strains. As seen for o -phase (Sec. III B), a unit cell with 12 atoms results in 36 vibrational modes, 3 for translation modes and 33 for optical phonon modes. In the case of $R3m$ space group, there are three different modes A_1 , A_2 , and E ; the irreducible representation at the Γ point is

$$\Gamma = 8A_1 + 3A_2 + 11E. \quad (12)$$

The A_1 and (degenerate) E modes are simultaneously Raman- and IR-active, while the A_2 modes are Raman-active and IR-inactive. The calculated A_1 mode frequencies are shown in Table IV for ZrO₂ and HfO₂; experimentally, no data are available for ZrO₂-HfO₂ in r -phase. The E and A_2 phonon frequencies are given in Table S.8 [67].

Following the same method as described in Secs. III A and III B, the EO coefficients obtained for ZrO₂ and HfO₂ r -phase are given in Table VII. Comparing these EO coefficients to the ones of LNO and o -phase, r -phase shows very modest EO values. This trend is also observed in terms of polarization obtained for r -phase compared to orthorhombic $Pbc2_1$ (Tables III and VI).

Strain dependence of EO coefficients

Because the ZrO₂-HfO₂ $R3m$ phase has a strong dependence on the compressive strain, the r_{33} EO coefficient of r -ZrO₂ is computed at different rhombohedral angles. The results are displayed in Fig. 4, showing a linear dependence of r_{33} with respect to the rhombohedral angle. Even at a high compressive strain (rhombohedral angle of 88°), the EO coefficient of the r -phase is still lower than the one calculated for o -ZrO₂. Two main reasons cause the low EO coefficients of r -ZrO₂ compared to o -ZrO₂. First is the relatively wider band gap in the r -phase, which reduces the electronic contribution. The second stems from the A_1 low-frequency phonon modes, which bring negligible contributions to EO coefficients in the r -phase, while similar modes contribute highly to the ones of the o -phase (see Sec. III B). In more detail, for the r -phase, out of the eight A_1 active modes (Table IV) only three modes at 220, 352, and 449 cm⁻¹ contribute significantly to r_{33} and r_{13} . The modes at 220 and 352 cm⁻¹ give almost the same value of

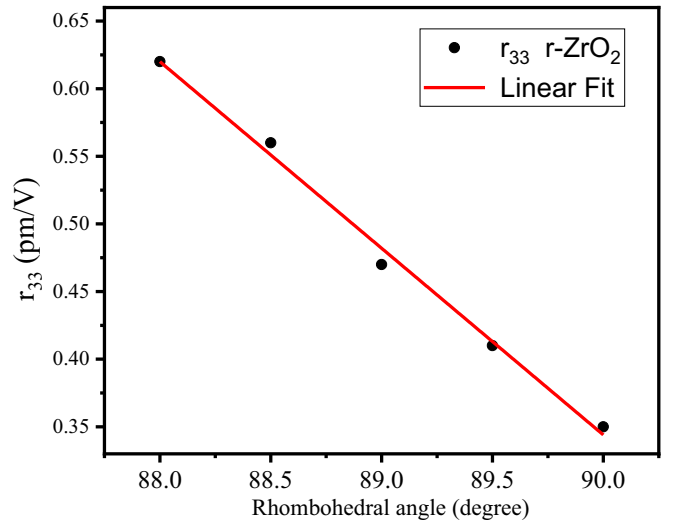


FIG. 4. r_{33} EO coefficient of r -ZrO₂ computed at different angles.

the hyperpolarizabilities β_{33} [Eq. (6)], but with opposite signs, hence they cancel each other. As a result, solely the mode at 449 cm⁻¹ is contributing to r_{33} . This is the most probable reason why the r -phase exhibits a lower EO coefficient than the o -phase. Finally, as illustrated in Fig. 3, this gives r -phase a very low figure of merit compared to o -phase and to LNO.

IV. CONCLUSION

In this work, we investigated the electro-optic Pockels coefficients of the ZrO₂ and HfO₂ compounds in two noncentrosymmetric phases: rhombohedral $R3m$ and orthorhombic $Pbc2_1$. We determined that the o -phase has considerably higher EO coefficients than the r -phase. This remains true for a highly strained rhombohedral phase; the optical nonlinearity is weak compared to the o -phase. Moreover, r_{33} and r_{13} in the orthorhombic phase are higher in ZrO₂ than in HfO₂, with values of about 12 and 7 pm/V for ZrO₂ and HfO₂, respectively. Comparisons between the EO coefficients of o -ZrO₂ and the rhombohedral LiNbO₃ reference material revealed that these materials share similar r_{13} coefficients. In contrast, the r_{33} coefficient of o -ZrO₂ is found to be three times lower than that of LiNbO₃. We observed that the polar and low-frequency phonon modes contribute most to the EO in the orthorhombic phase; the same trend is also observed in LiNbO₃. Our numerical results suggest that the ferroelectric orthorhombic phase of ZrO₂ and HfO₂-based thin films can be relevant for EO applications when considering their compatibility with silicon. Finally, considering the dominant contribution of the ionic part as identified in this work, we believe that doping ZrO₂/HfO₂ with a suitable element that stabilizes the orthorhombic phase and also increases the ionicity of these materials will lead to high EO coefficients, suitable for their use in photonic devices.

ACKNOWLEDGMENTS

This work has received support from the Agence Nationale de la Recherche (ANR) under project FOIST (No. ANR-18-CE24-0030), and from the French national

network RENATECH for nanofabrication. For part of this work, access was granted to the HPC resources of CCRT/CINES/IDRIS under the allocation 2021-2022 (AD010807031R1) made by GENCI (Grand Equipement

National de Calcul Intensif). We also acknowledge the “Direction du Numérique” of the “Université de Pau et des Pays de l’Adour” and the mésocentre Aquitain (MCIA) for their computing facilities.

-
- [1] A. K. Mohapatra, M. G. Bason, B. Butscher, K. J. Weatherill, and C. S. Adams, A giant electro-optic effect using polarizable dark states, *Nat. Phys.* **4**, 890 (2008).
- [2] A. Melikyan, L. Alloatti, A. Muslija, D. Hillerkuss, P. C. Schindler, J. Li, R. Palmer, D. Korn, S. Muehlbrandt, D. Van Thourhout, B. Chen, R. Dinu, M. Sommer, C. Koos, M. Kohl, W. Freude, and J. Leuthold, High-speed plasmonic phase modulators, *Nat. Photon.* **8**, 229 (2014).
- [3] A. Rueda, F. Sedlmeir, M. Kumari, G. Leuchs, and H. G. L. Schwefel, Resonant electrooptic frequency comb, *Nature (London)* **568**, 378 (2019).
- [4] S. Abel, F. Eltes, J. E. Ortmann, A. Messner, P. Castera, T. Wagner, D. Urbonas, A. Rosa, A. M. Gutierrez, D. Tulli, P. Ma, B. Baeuerle, A. Josten, W. Heni, D. Caimi, L. Czornomaz, A. A. Demkov, J. Leuthold, P. Sanchis, and J. Fompeyrine, Large Pockels effect in micro- and nanostructured bariumtitanate integrated on silicon, *Nat. Mater.* **18**, 42 (2019).
- [5] J. L. O’Brien, A. Furusawa, and J. Vučković, Photonic quantum technologies, *Nat. Photon.* **3**, 687 (2009).
- [6] J. Wang, F. Sciarrino, A. Laing, and M. G. Thompson, Integrated photonic quantum technologies, *Nat. Photon.* **14**, 273 (2020).
- [7] J. K. George, A. Mehrabian, R. Amin, J. Meng, T. Ferreira de Lima, A. N. Tait, B. J. Shastri, T. El-Ghazawi, P. R. Prucnal, and V. J. Sorger, Neuromorphic photonics with electroabsorption modulators, *Opt. Express* **27**, 5181 (2019).
- [8] Y. Shen, N. C. Harris, S. Skirlo, M. Prabhu, T. Baehr-Jones, M. Hochberg, X. Sun, S. Zhao, H. Larochelle, D. Englund, and M. Soljačić, Deep learning with coherent nanophotonic circuits, *Nat. Photon.* **11**, 441 (2017).
- [9] B. J. Offrein, J. Geler-Kremer, J. Weiss, R. Dangel, P. Stark, A. Sharma, S. Abel, and F. Horst, Prospects for photonic implementations of neuromorphic devices and systems, in *Proceedings of the IEEE International Electron Devices Meeting (IEDM), San Francisco* (IEEE, Piscataway, NJ, 2020), p. 7.4.1.
- [10] M. E. Lines and A. M. Glass, *Principles and Applications of Ferroelectrics and Related Materials* (Oxford University Press, Oxford, 2001), p. 694.
- [11] M. Zgonik, P. Bernasconi, M. Duelli, R. Schlessler, P. Gunter, M. H. Garrett, D. Rytz, Y. Zhu, and X. Wu, Dielectric, elastic, piezoelectric, electro-optic, and elasto-optic tensors of BaTiO₃ crystals, *Phys. Rev. B* **50**, 5941 (1994).
- [12] A. Messner, F. Eltes, P. Ma, S. Abel, B. Baeuerle, A. Josten, W. Heni, D. Caimi, J. Fompeyrine, and J. Leuthold, Plasmonic ferroelectric modulators, *J. Lightwave Technol.* **37**, 281 (2019).
- [13] C. Xiong, W. H. P. Pernice, J. H. Ngai, J. W. Reiner, D. Kumah, F. J. Walker, C. H. Ahn, and H. X. Tang, Active silicon integrated nanophotonics: Ferroelectric BaTiO₃ devices, *Nano Lett.* **14**, 1419 (2014).
- [14] T. Paoletta and A. A. Demkov, Pockels effect in low-temperature rhombohedral BaTiO₃, *Phys. Rev. B* **103**, 014303 (2021).
- [15] F. Eltes, G. E. Villarreal-Garcia, D. Caimi, H. Siegwart, A. A. Gentile, A. Hart, P. Stark, G. D. Marshall, M. G. Thompson, J. Barreto, J. Fompeyrine, and S. Abel, An integrated optical modulator operating at cryogenic temperatures, *Nat. Mater.* **19**, 1164 (2020).
- [16] E. H. Turner, High-frequency electro-optic coefficients of lithium niobate, *Appl. Phys. Lett.* **8**, 303 (1966).
- [17] E. L. Wooten, K. M. Kissa, A. Yi-Yan, E. J. Murphy, D. A. Lafaw, P. F. Hallemeier, D. Maack, D. V. Attanasio, D. J. Fritz, G. J. McBrien, and D. E. Bossi, A review of lithium niobate modulators for fiber-optic communications systems, *IEEE J. Sel. Top. Quantum Electron.* **6**, 69 (2000).
- [18] C. Wang, M. Zhang, X. Chen, M. Bertrand, A. Shams-Ansari, S. Chandrasekhar, P. Winzer, and M. Loncar, Integrated lithium niobate electro-optic modulators operating at CMOS compatible voltages, *Nature (London)* **562**, 101 (2018).
- [19] P. Rabiei, J. Ma, S. Khan, J. Chiles, and S. Fathpour, Heterogeneous lithium niobate photonics on silicon substrates, *Opt. Express* **21**, 25573 (2013).
- [20] T. S. Böske, J. Müller, D. Bräuhäus, U. Schröder, and U. Böttger, Ferroelectricity in hafnium oxide thin films, *Appl. Phys. Lett.* **99**, 102903 (2011).
- [21] Y. Wei, P. Nukala, M. Salverda, S. Matzen, H. J. Zhao, J. Momand, A. S. Everhardt, G. Agnus, G. R. Blake, P. Lecoeur, B. J. Kooi, J. Íñiguez, B. Dkhil, and B. Noheda, A rhombohedral ferroelectric phase in epitaxially strained Hf_{0.5}Zr_{0.5}O₂ thin films, *Nat. Mater.* **17**, 1095 (2018).
- [22] T. Ali, P. Polakowski, S. Riedel, T. Büttner, T. Kämpfe, M. Rudolph, B. Pätzold, K. Seidel, D. Löhr, R. Hoffmann, M. Czernohorsky, K. Kühnel, P. Steinke, J. Calvo, K. Zimmermann, and J. Müller, High endurance ferroelectric hafnium oxide-based FeFET memory without retention penalty, *IEEE Trans. Electron Devices* **65**, 3769 (2018).
- [23] J. Müller, T. S. Böske, D. Bräuhäus, U. Schröder, U. Böttger, J. Sundqvist, P. Kücher, T. Mikolajick, and L. Frey, Ferroelectric Zr_{0.5}Hf_{0.5}O₂ thin films for nonvolatile memory applications, *Appl. Phys. Lett.* **99**, 112901 (2011).
- [24] M. H. Park, H. J. Kim, Y. J. Kim, T. Moon, K. D. Kim, and C. S. Hwang, Thin Hf_xZr_{1-x}O₂ films: A new lead-free system for electrostatic supercapacitors with large energy storage density and robust thermal stability, *Adv. Energy Mater.* **4**, 1400610 (2014).
- [25] J. P. B. Silva, K. C. Sekhar, H. Pan, J. L. MacManus-Driscoll, and M. Pereira, Advances in dielectric thin films for energy storage applications, revealing the promise of group iv binary oxides, *ACS Energy Lett.* **6**, 2208 (2021).
- [26] D. K. Fork, F. Armani-Leplingard, and J. J. Kingston, Optical losses in ferroelectric oxide thin films: Is there light at the end of the tunnel?, *MRS Proc.* **361**, 155 (1994).
- [27] D. Sando, Y. Yang, C. Paillard, B. Dkhil, L. Bellaiche, and V. Nagarajan, Epitaxial ferroelectric oxide thin films for optical applications, *Appl. Phys. Rev.* **5**, 041108 (2018).

- [28] S. S. Cheema, D. Kwon, N. Shanker, R. Dos Reis, S. Hsu, J. Xiao, H. Zhang, R. Wagner, A. Datar, M. R. McCarter *et al.*, Enhanced ferroelectricity in ultrathin films grown directly on silicon, *Nature (London)* **580**, 478 (2020).
- [29] P. Polakowski and J. Müller, Ferroelectricity in undoped hafnium oxide, *Appl. Phys. Lett.* **106**, 232905 (2015).
- [30] S. Starschich, T. Schenk, U. Schroeder, and U. Boettger, Ferroelectric and piezoelectric properties of Hf_{1-x}Zr_xO₂ and pure ZrO₂ films, *Appl. Phys. Lett.* **110**, 182905 (2017).
- [31] R. Shimura, T. Mimura, A. Tateyama, T. Shimizu, T. Yamada, Y. Tanaka, Y. Inoue, and H. Funakubo, Preparation of 1 μ m thick Y-doped HfO₂ ferroelectric films on (111) Pt/TiO_x/SiO₂/(001)Si substrates by a sputtering method and their ferroelectric and piezoelectric properties, *Jpn. J. Appl. Phys.* **60**, 031009 (2021).
- [32] J. Lyu, I. Fina, R. Solanas, J. Fontcuberta, and F. Sánchez, Robust ferroelectricity in epitaxial Hf_{1/2}Zr_{1/2}O₂ thin films, *Appl. Phys. Lett.* **113**, 082902 (2018).
- [33] P. Jiao, J. Li, Z. Xi, X. Zhang, J. Wang, Y. Yang, Y. Deng, and D. Wu, Ferroelectric Hf_{0.5}Zr_{0.5}O₂ thin films deposited epitaxially on (110)-oriented SrTiO₃, *Appl. Phys. Lett.* **119**, 252901 (2021).
- [34] Y. Yun, P. Buragohain, M. Li, Z. Ahmadi, Y. Zhang, X. Li, H. Wang, J. Li, P. Lu, L. Tao, H. Wang, J. E. Shield, E. Y. Tsymlal, A. Gruverman, and X. Xu, Intrinsic ferroelectricity in Y-doped HfO₂ thin films, *Nat. Mater.* **21**, 903 (2022).
- [35] J. P. B. Silva, R. F. Negrea, M. C. Istrate, S. Dutta, H. Aramberri, J. Iniguez, F. G. Figueiras, C. Ghica, K. C. Sekhar, and A. L. Kholkin, Wake-up free ferroelectric rhombohedral phase in epitaxially strained ZrO₂ thin films, *ACS Appl. Mater. Interfaces* **13**, 51383 (2021).
- [36] A. El Boutaybi, T. Maroutian, L. Largeau, S. Matzen, and P. Lecoeur, Stabilization of the epitaxial rhombohedral ferroelectric phase in ZrO₂ by surface energy, *Phys. Rev. Mater.* **6**, 074406 (2022).
- [37] M. Hoffmann, M. Pešić, K. Chatterjee, A. I. Khan, S. Salahuddin, S. Slesazek, U. Schroeder, and T. Mikolajick, Direct observation of negative capacitance in polycrystalline ferroelectric HfO₂, *Adv. Funct. Mater.* **26**, 8643 (2016).
- [38] M. Hoffmann, S. Slesazek, T. Mikolajick, and C. S. Hwang, Negative capacitance in HfO₂- and ZrO₂-based ferroelectrics, in *Ferroelectricity in Doped Hafnium Oxide: Materials, Properties and Devices*, edited by U. Schroeder, C. S. Hwang, and H. Funakubo (Elsevier, Amsterdam, 2019), p. 473.
- [39] Y. Wei, S. Matzen, T. Maroutian, G. Agnus, M. Salverda, P. Nukala, Q. Chen, J. Ye, P. Lecoeur, and B. Noheda, Magnetic Tunnel Junctions Based on Ferroelectric Hf_{0.5}Zr_{0.5}O₂ Tunnel Barriers, *Phys. Rev. Appl.* **12**, 031001(R) (2019).
- [40] Y. Goh and S. Jeon, The effect of the bottom electrode on ferroelectric tunnel junctions based on CMOS-compatible HfO₂, *Nanotechnology* **29**, 335201 (2018).
- [41] S. Kondo, R. Shimura, T. Teranishi, A. Kishimoto, T. Nagasaki, H. Funakubo, and T. Yamada, Linear electro-optic effect in ferroelectric HfO₂-based epitaxial thin films, *Jpn. J. Appl. Phys.* **60**, 070905 (2021).
- [42] S. Kondo, R. Shimura, T. Teranishi, A. Kishimoto, T. Nagasaki, H. Funakubo, and T. Yamada, Influence of orientation on the electro-optic effect in epitaxial Y-doped HfO₂ ferroelectric thin films, *Jpn. J. Appl. Phys.* **60**, SFFB13 (2021).
- [43] R. Dovesi, A. Erba, R. Orlando, C. M. Zicovich-Wilson, B. Civalleri, L. Maschio, M. Rérat, S. Casassa, J. Baima, S. Salustro, and B. Kirtman, Quantum-mechanical condensed matter simulations with CRYSTAL, *WIREs Comput. Mol. Sci.* **8**, e1360 (2018).
- [44] L. Maschio, M. Rérat, B. Kirtman, and R. Dovesi, Calculation of the dynamic first electronic hyperpolarizability $\beta(-\omega_\sigma; \omega_1, \omega_2)$ of periodic systems. Theory, validation, and application to multi-layer MoS₂, *J. Chem. Phys.* **143**, 244102 (2015).
- [45] M. Rérat, L. Maschio, B. Kirtman, B. Civalleri, and R. Dovesi, Computation of Second Harmonic Generation for Crystalline Urea and KDP. An ab Initio Approach through the Coupled Perturbed Hartree-Fock/Kohn-Sham Scheme, *J. Chem. Theor. Comput.* **12**, 107 (2016).
- [46] D. M. Bishop, Molecular vibrational and rotational motion in static and dynamic electric fields, *Rev. Mod. Phys.* **62**, 343 (1990).
- [47] M. Ferrero, M. Rérat, R. Orlando, and R. Dovesi, The calculation of static polarizabilities of 1-3d periodic compounds. the implementation in the crystal code, *J. Comput. Chem.* **29**, 1450 (2008).
- [48] M. Ferrero, M. Rérat, B. Kirtman, and R. Dovesi, Calculation of first and second static hyperpolarizabilities of one- to three-dimensional periodic compounds. implementation in the crystal code, *J. Chem. Phys.* **129**, 244110 (2008).
- [49] M. Ferrero, M. Rérat, R. Orlando, R. Dovesi, and I. Bush, Coupled perturbed kohn-sham calculation of static polarizabilities of periodic compounds, *J. Phys.: Conf. Ser.* **117**, 012016 (2008).
- [50] P. Otto, Calculation of the polarizability and hyperpolarizabilities of periodic quasi-one-dimensional systems, *Phys. Rev. B* **45**, 10876 (1992).
- [51] A. Erba, M. T. Ruggiero, T. M. Korter, and R. Dovesi, Piezoelectric tensor of crystals from quantum-mechanical calculations, *J. Chem. Phys.* **143**, 144504 (2015).
- [52] M. Jazbinšek and M. Zgonik, Material tensor parameters of LiNbO₃ relevant for electro and elasto-optics, *Appl. Phys. B* **74**, 407 (2002).
- [53] A. Erba and R. Dovesi, Photoelasticity of crystals from theoretical simulations, *Phys. Rev. B* **88**, 045121 (2013).
- [54] F. Pascale, C. M. Zicovich-Wilson, F. López Gejo, B. Civalleri, R. Orlando, and R. Dovesi, The calculation of the vibrational frequencies of crystalline compounds and its implementation in the crystal code, *J. Comput. Chem.* **25**, 888 (2004).
- [55] C. M. Zicovich-Wilson, F. Pascale, C. Roetti, V. R. Saunders, R. Orlando, and R. Dovesi, Calculation of the vibration frequencies of α -quartz: The effect of Hamiltonian and basis set, *J. Comput. Chem.* **25**, 1873 (2004).
- [56] L. Maschio, B. Kirtman, M. Rérat, R. Orlando, and R. Dovesi, Comment on "Ab initio analytical infrared intensities for periodic systems through a coupled perturbed Hartree-Fock/Kohn-Sham method" [J. Chem. Phys. 137, 204113 (2012)], *J. Chem. Phys.* **139**, 167101 (2013).
- [57] A. D. Becke, Density-functional thermochemistry. III. The role of exact exchange, *J. Chem. Phys.* **98**, 5648 (1993).
- [58] C. Lee, W. Yang, and R. G. Parr, Development of the collesalvetti correlation-energy formula into a functional of the electron density, *Phys. Rev. B* **37**, 785 (1988).
- [59] J. P. Perdew, K. Burke, and M. Ernzerhof, Generalized Gradient Approximation Made Simple, *Phys. Rev. Lett.* **77**, 3865 (1996).

- [60] C. Adamo and V. Barone, Toward reliable density functional methods without adjustable parameters: The PBE0 model, *J. Chem. Phys.* **110**, 6158 (1999).
- [61] S. Dall’Olio, R. Dovesi, and R. Resta, Spontaneous polarization as a berry phase of the hartree-fock wave function: The case of KNbO_3 , *Phys. Rev. B* **56**, 10105 (1997).
- [62] D. Vilela Oliveira, J. Laun, M. F. Peintinger, and T. Bredow, BSSE-correction scheme for consistent gaussian basis sets of double- and triple-zeta valence with polarization quality for solid-state calculations, *J. Comput. Chem.* **40**, 2364 (2019).
- [63] R. P. McCall, E. M. Scherr, A. G. MacDiarmid, and A. J. Epstein, Anisotropic optical properties of an oriented-emeraldine-base polymer and an emeraldine-hydrochloride-salt polymer, *Phys. Rev. B* **50**, 5094 (1994).
- [64] L. Valenzano, B. Civalieri, S. Chavan, S. Bordiga, M. H. Nilsen, S. Jakobsen, K. P. Lillerud, and C. Lamberti, Disclosing the complex structure of UiO-66 metal-organic framework: A synergic combination of experiment and theory, *Chem. Mater.* **23**, 1700 (2011).
- [65] T. Bredow, K. Jug, and R. A. Evarestov, Electronic and magnetic structure of ScMnO_3 , *Phys. Status Solidi B* **243**, R10 (2006).
- [66] D. Muñoz Ramo, J. L. Gavartin, A. L. Shluger, and G. Bersuker, Spectroscopic properties of oxygen vacancies in monoclinic HfO_2 calculated with periodic and embedded cluster density functional theory, *Phys. Rev. B* **75**, 205336 (2007).
- [67] See Supplemental Material at <http://link.aps.org/supplemental/10.1103/PhysRevB.107.045140> for more details on EO and second-harmonic-generation symmetry and complementary results on phonon modes of LNO and $\text{ZrO}_2\text{-HfO}_2$, crystal structure, and atomic positions. It includes Refs. [16,73,77–79,82,83,86–89].
- [68] A. Dhar and A. Mansingh, Optical properties of reduced lithium niobate single crystals, *J. Appl. Phys.* **68**, 5804 (1990).
- [69] C. Thierfelder, S. Sanna, A. Schindlmayr, and W. G. Schmidt, Do we know the band gap of lithium niobate? *Phys. Status Solidi C* **7**, 362 (2010).
- [70] H. H. Nahm and C. H. Park, First-principles study of microscopic properties of the Nb antisite in LiNbO_3 : Comparison to phenomenological polaron theory, *Phys. Rev. B* **78**, 184108 (2008).
- [71] U. Schlarb and K. Betzler, Refractive indices of lithium niobate as a function of wavelength and composition, *J. Appl. Phys.* **73**, 3472 (1993).
- [72] J. G. Bergman, A. Ashkin, A. A. Ballman, J. M. Dziedzic, H. J. Levinstein, and R. G. Smith, Curie temperature, birefringence, and phase-matching temperature variations in LiNbO_3 as function of melt stoichiometry, *Appl. Phys. Lett.* **12**, 92 (1968).
- [73] M. Veithen, X. Gonze, and P. Ghosez, First-Principles Study of the Electro-Optic Effect in Ferroelectric Oxides, *Phys. Rev. Lett.* **93**, 187401 (2004).
- [74] D. F. Nelson and R. M. Mikulyak, Refractive indices of congruently melting lithium niobate, *J. Appl. Phys.* **45**, 3688 (1974).
- [75] To compare our results and those of Veithen *et al.* [73], one should note the following points: (i) For the crystal orientation chosen in the current study, r_{22} is replaced by r_{11} with the same absolute value and a negative sign; (ii) while Veithen *et al.* carried out their computations at infinite wavelength, different from the 633 nm wavelength used in our study, this should not have a major influence on the EO coefficients (see Figs. 2 and S2 [67]). Therefore, our outcomes obtained with hybrid functionals and basis sets of crystalline Gaussian type orbitals within the CPHF/KS approximation can be directly compared to the absolute values of the LDA coefficients reported in Ref. [73]. One should keep in mind that in the case of semi-conducting materials, nonhybrid functionals are expected to overshoot the electronic part of $\chi_{ijk}^{(2)}$, while pure DFT functionals return weaker soft phonon frequencies (see Table S3 [67]).
- [76] L. Maschio, B. Kirtman, M. Rérat, R. Orlando, and R. Dovesi, Ab initio analytical Raman intensities for periodic systems through a coupled perturbed Hartree-Fock/Kohn-Sham method in an atomic orbital basis. I. Theory, *J. Chem. Phys.* **139**, 164101 (2013).
- [77] K. K. Wong, *Properties of Lithium Niobate* (IEE, INSPEC, London, 2002), p. 136.
- [78] A. Rauber, *Current Topics in Materials Science*, edited by E. Kaldis (North-Holland, Amsterdam, 1978), Vol. 1, p. 481.
- [79] F. Abdi, M. Aillerie, P. Bourson, M. D. Fontana, and K. Polgar, Electro-optic properties in pure LiNbO_3 crystals from the congruent to the stoichiometric composition, *J. Appl. Phys.* **84**, 2251 (1998).
- [80] P. Giannozzi, S. Baroni, N. Bonini, M. Calandra, R. Car, C. Cavazzoni, D. Ceresoli, G. L. Chiarotti, M. Cococcioni, and I. Dabo *et al.*, QUANTUM ESPRESSO: A modular and open-source software project for quantum simulations of materials, *J. Phys.: Condens. Matter* **21**, 395502 (2009).
- [81] R. Materlik, C. Kunneth, and A. Kersch, The origin of ferroelectricity in $\text{Hf}_{1-x}\text{Zr}_x\text{O}_2$: A computational investigation and a surface energy model, *J. Appl. Phys.* **117**, 134109 (2015).
- [82] M. Materano, P. Reinig, A. Kersch, M. Popov, M. Deluca, T. Mikolajick, U. Boettger, and U. Schroeder, Raman spectroscopy as a key method to distinguish the ferroelectric orthorhombic phase in thin ZrO_2 based films, *Physica Status Solidi (RRL)* **16**, 2100589 (2022).
- [83] A. Yariv and P. Yeh, *Photonics: Optical Electronics in Modern Communications*, 6th ed. (Oxford University Press, Oxford, 2007).
- [84] E. H. Kisi and C. J. Howard, Crystal structures of zirconia phases and their inter-relation, *Key Eng. Mater.* **153-154**, 1 (1998).
- [85] E. H. Kisi, Influence of hydrostatic pressure on the $t \rightarrow o$ transformation in mg-psz studied by in situ neutron diffraction, *J. Am. Ceram. Soc.* **81**, 741 (1998).
- [86] I. Inbar and R. E. Cohen, Comparison of the electronic structures and energetics of ferroelectric LiNbO_3 and LiTaO_3 , *Phys. Rev. B* **53**, 1193 (1996).
- [87] V. Caciuc, A. V. Postnikov, and G. Borstel, Ab initio structure and zone-center phonons in LiNbO_3 , *Phys. Rev. B* **61**, 8806 (2000).
- [88] S. Kojima, Composition variation of optical phonon damping in lithium niobate crystals, *Jpn. J. Appl. Phys.* **32**, 4373 (1993).
- [89] R. Claus, J. Brandmüller, G. Borstel, E. Wiesendanger, and L. Steffan, Directional Dispersion and Assignment of Optical Phonons in LiNbO_3 , *Z. Naturforsch. A* **27**, 1187 (1972).